J. Fluid Mech. (2006), *vol.* 555, *pp.* 363–385.
doi:10.1017/S0022112006009529 Printed in the United Kingdom

The far downstream evolution of the high-Reynolds-number axisymmetric wake behind a disk. Part 1. Single-point statistics

By PETER B. V. JOHANSSON AND WILLIAM K. GEORGE

Turbulence Research Laboratory, Department of Applied Mechanics, Chalmers University of Technology, Gothenburg, SE-412 96, Sweden

(Received 22 November 2004 and in revised form 4 November 2005)

The high-Reynolds-number axisymmetric wake behind a disk has been studied for $10 \leqslant x/D \leqslant 150$ ($36 \leqslant x/\theta \leqslant 552$) using a rake of 15 hot wires. The disk had a diameter of 20 mm, and the Reynolds number based on the free-stream velocity was 26 400. Mean velocity profiles, root-mean-square profiles, and power spectra are presented. By using regression techniques to fit the velocity profiles it was possible to obtain accurate velocity centreline deficits and transverse length scales to even the last downstream position. Beyond the initial region which extends to $x/D = 30$, the data are in excellent agreement with the high-Reynolds-number equilibrium similarity solution.

1. Introduction

The axisymmetric far wake is a very challenging flow to investigate experimentally, since the velocity differences of interest are very small. A sketch of the axisymmetric wake together with the coordinate system used in this study is shown in figure 1. The mean velocity deficit at the centreline is here defined as $U_o = U_\infty - U_{CL}$. The Reynolds decomposition is applied, and averaged values are denoted with upper-case letters, and fluctuating quantities with lower-case letters. It has been found experimentally that U_o falls rapidly downstream from about 10 % of the free-stream velocity at $x/D = 10$ to about 1 % of the free-stream velocity at the farthest downstream position in this experiment ($x/D = 150$). The root mean square of the fluctuations, u', is of the same order as the velocity deficit, i.e. $u'/U_o \approx 1$. These low levels place extreme demands on the wind tunnel, both in terms of its length and flow quality. Moreover, this rules out the use of most laser-based techniques, like laser Doppler anemometry (LDA), or particle image velocimetry (PIV) which simply do not have enough resolution. The only measurement technique that is capable of resolving such weak fluctuations is hot-wire anemometry, but even this technique has accuracy limitations. These are discussed herein, and a method to account for them is provided.

2. Basic equations

The Reynolds-averaged momentum equations for the axisymmetric far wake without swirl and with a negligible free-stream pressure gradient reduce to first order to a balance between the advection of the velocity deficit and the radial gradient of the Reynolds stress:

$$U_\infty \frac{\partial}{\partial x}(U - U_\infty) = -\frac{1}{r}\frac{\partial}{\partial r}(r\overline{uv}). \tag{2.1}$$

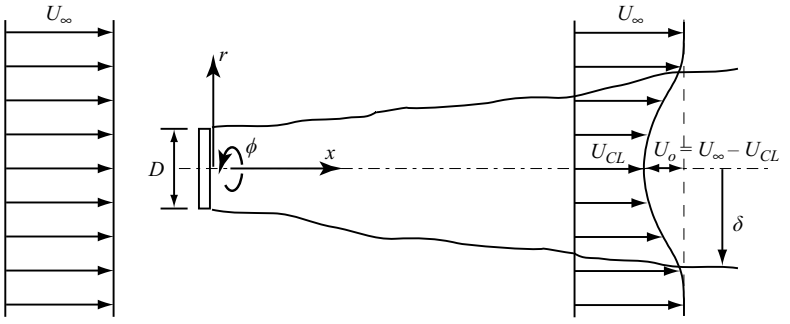

FIGURE 1. Axisymmetric wake coordinates.

The viscous term has been neglected, since only high-Reynolds-number flows are of interest here. (Note that Johansson, George & Gourlay (2003) consider also viscous solutions to this equation.)

The momentum equation can be integrated over a cross-section to yield an integral constraint, i.e. the conservation of momentum:

$$U_\infty \int_0^\infty (U_\infty - U)\, r\, \mathrm{d}r \cong \theta^2 U_\infty^2, \tag{2.2}$$

where θ is the momentum thickness. This equation is satisfied to within a few percent beyond $x/D = 10$. It is only valid for a zero free-stream pressure gradient in the wind tunnel. This may not be the case in reality, and an analysis of the possible effect of a pressure gradient is provided in Appendix A. Note that the definition of the 'true' θ is

$$\theta^2 = \lim_{\tilde{r}\to\infty} \frac{1}{U_\infty^2} \int_0^{\tilde{r}} U(U_\infty - U)\, r\, \mathrm{d}r. \tag{2.3}$$

A convenient choice for the transverse length scale is

$$\delta_*^2 = \lim_{\tilde{r}\to\infty} \frac{1}{U_o} \int_0^{\tilde{r}} (U_\infty - U)\, r\, \mathrm{d}r. \tag{2.4}$$

The advantage of this particular choice is that it satisfies equation (2.2) exactly, i.e.

$$U_o \delta_*^2 = U_\infty \theta^2. \tag{2.5}$$

These equations together with the transport equations for Reynolds stresses and an equilibrium similarity hypothesis yield what Johansson *et al.* (2003) called the high-Reynolds-number similarity solution for the wake growth (which corresponds to the classical cube root solution), i.e.

$$\delta_* \sim x^{1/3}. \tag{2.6}$$

It should be noted that this is not the only possible similarity solution and that certain conditions have to be fulfilled for this solution to be found in an experiment at all. These are discussed in detail by Johansson *et al.* (2003). Also, Johansson *et al.* (2003) noted that the coefficients in general depend on the wake generator.

3. Historical review

Using hot-wire anemometry, Carmody (1964) presented the findings of an experiment on a circular disk oriented perpendicular to the flow at a Reynolds number

based on the disk diameter and free-stream velocity (Re) of 70 000. He presented mean velocity, root-mean-square fluctuations, and Reynolds stress profiles, as well as streamwise wake growth. Shortly thereafter, Hwang & Baldwin (1966) presented measured turbulence intensities and wake growth for a large span of downstream locations, $x/D = 5$ to $x/D \approx 900$ behind various circular disks. Curiously, they did not present the centreline mean velocity decay. The reliability of the hot-wire technique was discussed thoroughly in their paper, but the accuracy in terms of a percentage was not given. Both sets of data show significant scatter, most likely closely linked to the capability of the hot-wire anemometers used at that time. Hwang & Baldwin (1966) even reported difficulties in reproducing their own results on a day-to-day basis.

Gibson, Chen & Lin (1968) presented mean velocity and turbulence intensity profiles for a sphere wake at a Reynolds number of 65 000 using hot wires and Pitot tubes. The investigation covered only downstream distances to $x/D = 60$, but they stated that the root-mean-square fluctuations of the velocity were of the same order as the mean velocity deficit to within the accuracy of the experiment. They credited this finding to Cooper & Lutzky (1955) who performed an experiment on a disk wake.

Uberoi & Freymuth (1970) measured the sphere wake at a Reynolds number of 8600. Their investigation covered a downstream distance up to $x/D = 150$, but their presented results on the mean velocity deficit only go to $x/D = 100$. They did, however, claim that their data behaved according to the classical cube root solution, if the virtual origin was chosen appropriately. But they showed no downstream variation of either the centreline deficit or wake width, and showed only two collapsed profiles at $x/D = 50$ and 100.

In none of these experiments (Carmody 1964; Hwang & Baldwin 1966; Gibson *et al.* 1968), was the conservation of momentum addressed. This was, however, thoroughly investigated by Cannon (1991). He examined both the integral and differential mean momentum equations, and showed that his mean velocity and Reynolds stress data satisfied both for five different wake generators (disk, sphere and three porous disks with different porosity). The common denominator of these flows was that they had the same drag, which is why conservation of momentum was important. The Reynolds number based on diameter varied between 13 000 for the solid disk, 14 000–17 000 for the screens, and 21 500 for the sphere. The measurements extended over a range of x/D of about 10 to 125. Unfortunately, however, it was not clear that any of the wakes achieved a region downstream where u'/U_o appeared constant.

Johansson, George & Woodward (2002) studied the axisymmetric disk wake using a rake of 13 hot wires in order to obtain two-point cross-spectra in cross-sections of the flow from $x/D = 10$ to $x/D = 50$. These two-point cross-spectra were then used in the kernel of a proper orthogonal decomposition to extract the energetic features of the flow in a manner similar to Part 2 of this paper (Johansson & George 2006). Johansson noted that their mean velocity profiles were affected by thermal drift of the anemometers. The centreline mean velocity deficit, U_o, was about 3 % of the free-stream velocity at the farthest downstream location.

The present investigation extends the study in Johansson *et al.* (2002) to a greatly increased distance downstream (to $x/D = 150$) using a different facility. Here the influence of the thermal drift in the anemometers is even more pronounced, because of the smaller centreline deficit and accompanying low turbulence intensity. A thorough investigation of the accuracy of the measured data and a method of handling flows with such a small velocity difference is presented here. By using regression techniques

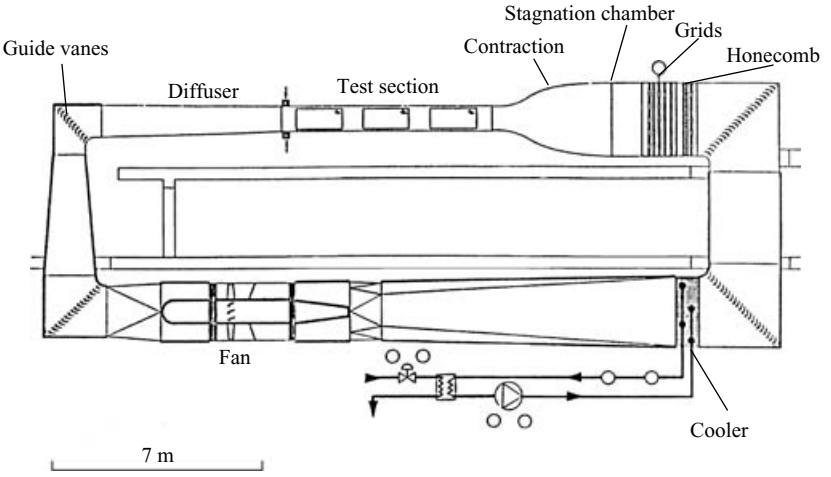

FIGURE 2. Wind Tunnel MTL at KTH, from Johansson (1992).

to fit the profiles and using momentum conservation as a requisite condition, it is shown to be possible to obtain reliable results much farther downstream than previously.

The data described here have been used by Johansson *et al.* (2003), together with the extensive DNS data of Gourlay *et al.* (2001), as a part of a general reanalysis of axisymmetric wakes. Their equilibrium similarity considerations showed the existence of two similarity regimes, both possibly retaining an asymptotic dependence on upstream conditions. Criteria were established there for when the initial transients die off, when the high-Reynolds-number solution might be expected, and when the low-Reynolds-number solution might emerge. Almost none of the earlier experiments described above satisfied these criteria. Both the data described here and the DNS data, however, show evidence for the high-Reynolds-number solution. Only the DNS data, though, evolves far enough downstream for the low-Reynolds-number solution to emerge.

4. Experimental setup

4.1. *Facility*

The experiment presented in this paper was performed in the MTL wind tunnel at the Royal Institute of Technology (KTH) in Stockholm, Sweden. The MTL tunnel, shown schematically in figure 2, is of closed loop type and is very suitable for measuring low-turbulence-intensity flows like the axisymmetric wake because of its relatively long test section and high flow quality. The streamwise free-stream turbulence intensity is lower than 0.03 %, and the cross-stream turbulence intensities are less than 0.06 %. The tunnel has a temperature uniformity in the test section of $\pm 0.2\,^{\circ}\mathrm{C}$. The test section has an area of $1.2 \times 0.8\ \mathrm{m}^2$ and the downstream length is 7 m. Further characteristics of the tunnel can be found in Johansson (1992). The tunnel was designed with primary focus on boundary layer measurements, so the desired pressure gradient in the measuring section is set by adjusting the roof. For this experiment the roof was aligned with the floor to ensure that the wake was kept straight throughout the experiment. The combination of wake growth and wall boundary layer growth could

D (mm)	θ (mm)	U_∞ (m s^{-1})	T (°C)	ν (m^2 s^{-1})	ρ (kg m^{-3})
20	5.4	20.1	20.4	15.2×10^{-6}	1.189

TABLE 1. Summary of experiment variables.

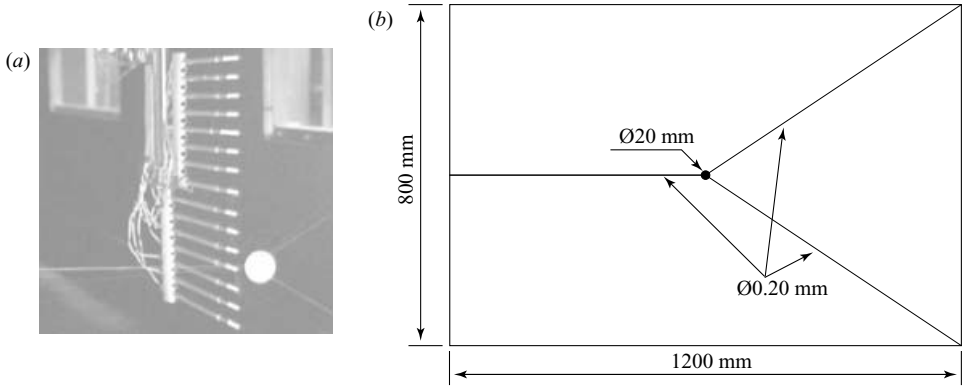

FIGURE 3. (*a*) Probe rake and disk, and (*b*) disk suspension in the cross-section in the MTL. wind tunnel at KTH

have caused a small (less than 1 %) but undesirable acceleration or deceleration of the free stream, the possible influence of which is investigated in Appendix A.

The wind tunnel velocity was monitored using a Pitot tube connected to a Furness FCO510 electronic manometer. The manometer was equipped with an absolute pressure sensor and a temperature sensor to provide the value of the velocity via the RS232 port directly to the computer. The velocity was monitored throughout the experiment and kept constant at 20.1 ± 0.05 m s^{-1}, resulting in a Reynolds number based on the free-stream velocity and disk diameter of 26 400. The measurements were automated using the integrated traverse and wind-tunnel speed control of the MTL. The experimental variables are summarized in table 1.

4.2. *Probe configuration*

The sensing device was composed of two rakes consisting of 15 hot wires in total. The primary reason for using rakes of probes was to be able to compute the numerous two-point cross-spectral quantities as described in Part 2 of this paper. The simultaneous measurement at many points made it possible to overcome the intrinsic limitation of the instrumentation. The rakes and probes, shown in figure 3(*a*), were constructed in-house at the Turbulence Research Laboratory of Chalmers. The rakes were made of steel airfoil profiles with a maximum thickness of 10 mm and a chord of 25 mm. The lower rake is fixed, while the upper can be rotated around the axis of the centre probe. The rotation allows an angular separation of the rakes between 15° and 335° with an accuracy of $\pm 1°$. The probe holders were fixed to the wings and were made of brass telescopic tubing with an outer diameter of 4 mm. The probe body was attached at the end of the probe holder. The probe body consisted of a brass tube with an outer diameter of 3.2 mm, containing a ceramic tubing with an outer diameter of 2.4 mm for prong insulation. Inside the ceramic tube, 0.4 mm steel piano wires were used as prongs, protruding 8 mm from the ceramic tube. The ends of the prongs were sharpened in order to reduce the effects of the prongs on the sensing wire. The

total distance between the movable steel wing and the sensing wire was 195 mm. The sensing wire was made of tungsten with diameter 5 μm (Sigmund-Cohn, Mt. Vernon, NY) and length 3 mm.

4.3. *Anemometers and data aquisition*

The anemometers consisted of a five-channel AA Lab Systems AN1003 constant-temperature anemometer that was available at KTH. For the remaining channels, nine DANTEC Miniature-CTA 54T30 were used. The differing thermal drifts of these anemometers considerably complicated their use, as will be discussed in detail later.

The data were digitized using an IO Tech Wavebook 516 16 bit 1 MHz sample and hold A/D converter, with an expansion module to enable 16 channels simultaneous sample and hold, connected to the computer via a fast parallel port PCI board. For the power spectra measured at downstream locations $x/D = 30$, 50, 70, 90, 110, 130, and 150, the signals were sampled at 4 kHz, consistent with the wire length cut-off, U_∞/l_w. This cut-off of the spectra well into the inertial subrange was intentional since the primary purpose of the experiment was to apply the proper orthogonal decomposition (POD) to determine the evolution of the energy-containing scales. Measurements were made simultaneously for all 15 probes. Each data block had 4096 samples, and a total of 360 blocks of data was taken per probe for each angular probe rake location. This large amount of data yields a variability of the power spectra at each radial position of 1.08 %.

For the single-point statistics, mean velocity and r.m.s. velocity, separate scans of the flow were made for the downstream locations $x/D = 10, 20, \ldots, 150$ using fewer blocks. For these runs, no spectral quantities were evaluated, so the sampling frequency was reduced to 1 kHz and only 60 blocks of 1000 samples were taken. This gives a statistical uncertainty of the mean velocity of at most 0.1 % (for the nearest downstream position where $u'/U \approx 10\,\%$). For the root mean square of the fluctuations, the statistical uncertainty is around 0.6 %.

4.4. *Disk suspension*

The disk had a diameter of 20 mm, a thickness of 2 mm with sharp edges, and was made of acrylic. It was suspended with three pairs of steel wires, each of diameter 0.2 mm. The disk was placed 1 m into the measuring section to allow for probe calibration upstream of the disk, and to avoid any possible small continuing acceleration of the flow near the contraction. The mounted disk in the test section is depicted in figure 3, which also shows the rake of probes downstream of it. The disk was centred by adjusting the tension of the supporting wires. By using pairs of support wires, the planar orientation of the disk could also be adjusted, since the tension of each support wire could be set individually. The final tuning of the disk centring was achieved by several preliminary test measurements, where the velocity field was measured for all available angular positions of the movable rake. The disk was moved based on the input from these velocity measurements and the procedure was repeated until a satisfactory result was achieved. For reasons that will be discussed in detail later, the centring was not performed using mean velocity distributions only, but instead was based on obtaining reasonably similar profiles of u' and power spectra for locations on either side of the plane $\Delta\theta = 180^\circ$ (i.e. it was moved until the u' values and the power spectra compared well for the angular separations of $\Delta\theta = 120^\circ$ and $\Delta\theta = 240^\circ$). (See figure 4 for the definition of the separation angle.) At the same time, it was ensured that the flow was indeed axisymmetric to within experimental accuracy.

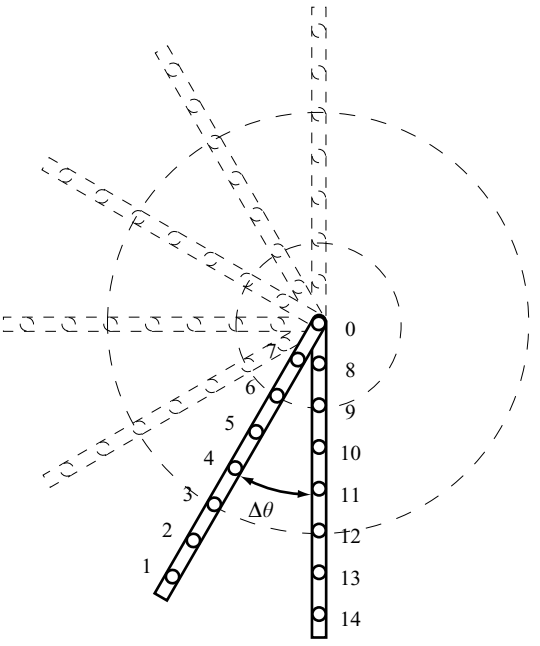

FIGURE 4. Map of traverse scheme, shown in increments of $\Delta\theta = 30°$.

The effects of the disk support wires were of considerable interest in ensuring that the energy distribution of the POD modes were not affected by them. In Johansson *et al.* (2002), four pairs of support wires were used. With such a configuration, the disk centring is easier, but it also creates a problem. Four pairs of support wires preclude some angular positions for the movable probe rake to be used without the velocity measurements being affected by the wakes of the supporting wires. The symmetry of the flow cannot be used to overcome this problem. The effect on the POD modes of the disk suspension method is further discussed in Part 2. In the three-support wire configuration used throughout this investigation, the wakes of the support wires did not affect the velocity measurements at any angular position of the movable probe rake, since the asymmetrical positioning of the support wires allowed replacement of the $\Delta\theta = 90°$ measuring position by the one at $\Delta\theta = 270°$.

4.5. *Spatial resolution*

The arrays were used in the same manner as Glauser & George (1987) and Johansson *et al.* (2002) to obtain the single-point statistics and two-point velocity cross-spectra for all combinations of locations shown in figure 4, 8820 in total at 1260 different positions. The measurement grid was originally chosen so that the angular resolution was acceptable for obtaining azimuthal Fourier transforms of the cross-spectra. This aspect is further discussed in Part 2. The movable array of probes was traversed from a 15° separation up to 180° with 15° increments in $\Delta\theta$. The 15° separation was chosen since it is approximately half the azimuthal integral scale, a methodology recently confirmed to be adequate by Gamard *et al.* (2002) in a jet, using both rakes of probes like those used here, and also a 139-hot-wire array of very long wires especially designed to reduce spatial aliasing. The numbering of the probes is shown in figure 4, with each hot-wire probe marked by a circle. The radial spacing of the probes beginning at the centre probe numbered 0 at $r = 0$ was 93, 80, 67, 54, 41, 28, 14 mm

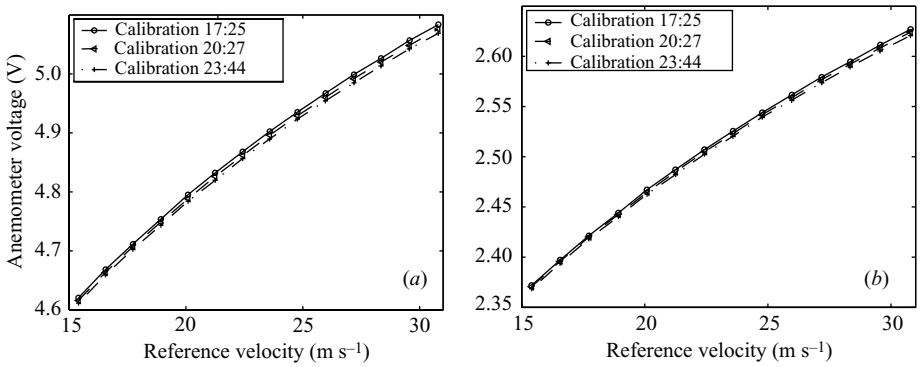

FIGURE 5. Calibration curves for (*a*) AN1003 and (*b*) DANTEC 54T30. Calibrations before, in the middle, and after the experiments for two downstream positions of measurement.

for probes numbered 1 to 7 on the movable rake, and −14, −28, −41, −54, −67, −80, −93 mm for the probes numbered 8 to 15 on the fixed rake. Negative values of r are used for distinguishing the probes on the fixed rake from those of the movable. Probes 0, 1, 3, 5, and 6 were connected to the AN1003 anemometer channels, while the others were connected to the DANTEC 54T30 anemometers.

The mean velocity and r.m.s. profiles were obtained with the rakes kept at the angular separation of $\Delta\theta = 180°$. To add more points in the velocity profiles, the rake was traversed in the direction of positive r an amount of 5 and 10 mm for these data sets.

5. Single-point statistics

5.1. *The mean velocity*

Obtaining the mean velocity profiles was by far the most difficult part of this entire experiment. The accuracy of the results of an experiment using hot wires is very sensitive to the reliability of the calibration, but this is not the major source of error in this investigation. Here, fourth-order polynomials were used to map the voltage output of the anemometer into velocity, as discussed by George, Beuther & Shabbir (1989). (Because of the low turbulence intensity, u'/U_∞, any lower-order polynomial would probably have worked just as well, as long as the range of velocities encountered was not outside the range of calibration.) The relative error of the calibration was less than $\pm 0.02\,\%$ over the range of velocities in the actual measurement.

The primary source of difficulty in the experiment was the thermal drift of the anemometers, especially from the offset amplifiers. This problem is easily overlooked when measuring flows with large velocity differences (e.g. a boundary layer or a jet) but is immediately obvious in a 'weak' turbulent flow like the axisymmetric wake. This was previously noted by Johansson *et al.* (2002), who stated that this mainly affected the mean velocity, leaving the root mean square of the velocity unaffected. This problem is more pronounced here than in the earlier study because the distance downstream is greater (150 disk diameters vs. 50) and the mean velocity deficit and r.m.s. velocity are much lower (1 % in the present vs. 3 % in the previous study). Part of the problem was solved by setting the troublesome anemometer offsets to zero, but the anemometers still drifted.

Figure 5 shows typical calibrations for both types of anemometer (AN1003 and 54T30) used. The different times correspond to calibrations before, in between, and

x/D	U_∞	U_{CL}	U_o	u'_{max}	u'_{max}/U_o	δ_*	$U_o\delta_*/\nu$
10	20.26	18.30	1.96	1.67	0.85	17.46	2252
20	20.25	19.25	1.00	1.05	1.05	24.45	1607
30	20.21	19.52	0.70	0.79	1.13	29.25	1341
40	20.19	19.63	0.56	0.65	1.15	32.48	1206
50	20.16	19.69	0.47	0.56	1.17	35.41	1105
60	20.14	19.72	0.42	0.49	1.15	37.48	1043
70	20.13	19.74	0.38	0.44	1.14	39.37	992
80	20.13	19.78	0.35	0.39	1.12	41.12	950
90	20.15	19.82	0.32	0.36	1.13	42.82	913
100	20.17	19.87	0.30	0.34	1.12	44.31	884
110	20.18	19.90	0.28	0.32	1.12	45.97	852
120	20.23	19.96	0.26	0.30	1.11	47.47	827
130	20.28	20.03	0.25	0.28	1.13	49.13	801
140	20.30	20.05	0.24	0.27	1.10	49.53	795
150	20.36	20.12	0.24	0.26	1.09	50.37	784

TABLE 2. Values of U_∞, U_{CL}, U_o and δ_* inferred from regression fit to profiles (see text and Appendix B); u'_{max} directly measured. Velocities in m s^{-1} and δ_* in mm.

after the experiments at two downstream positions. Although the differences in calibration before and after are slight, these differences are significant compared to the mean velocity deficit. This most certainly is the reason for the scatter of profiles in previous investigations (or perhaps even the complete absence of profiles from many). One significant advantage, however, is that equation (2.5) must be satisfied at and beyond $x/D \approx 10$ (i.e. momentum is conserved).

The method applied here to overcome these difficulties is presented in detail in Appendix B. The method considers data sets from all measured positions at a given downstream location simultaneously. It assumes only that the anemometers drift together (which was certainly true for the mini-Dantecs), so that the measured profile shifts uniformly in time. The method can be summarized as:

(*a*) A hypothesis of a general velocity profile is made. This profile has only a single length scale, δ_*, and velocity scale, $U_o = U_\infty - U_{CL}$, and both were assumed unknown for each profile, as was the free-stream velocity, U_∞.

(*b*) This profile is regressively fitted to each velocity profile at every downstream location for both rakes, requiring only conservation of momentum.

(*c*) The considerations of Appendix A make it clear that the slight variation of the computed U_∞ (of table 1) could at most be responsible for a 0.1 % variation of the momentum integral, thus verifying *a posteriori* its assumed constancy in (*b*) above.

Since the rake does not unambiguously cover the whole wake for the farthest downstream positions, the mean velocity deficit must be treated as an unknown quantity, but is linked to the transverse length scale through the conservation of momentum, equation (2.5). The method also provides as a bonus the necessary scaling parameters: the velocity deficit scale, U_o, and the wake width, δ_*. The evolution of these quantities is summarized in table 2.

The resulting corrected mean velocity profiles, normalized with the free-stream velocity for the downstream positions $x/D = 10$, 20, 30, 40, and 50 are shown in figure 6. Also shown next to the plots of the mean velocity deficit are the corresponding normalized turbulence intensities which will be discussed in the next section. The mean velocity deficit decreases rapidly initially, from about 9.5 % at $x/D = 10$, to 2.2 % at $x/D = 50$. The points in the velocity profiles associated with negative r were

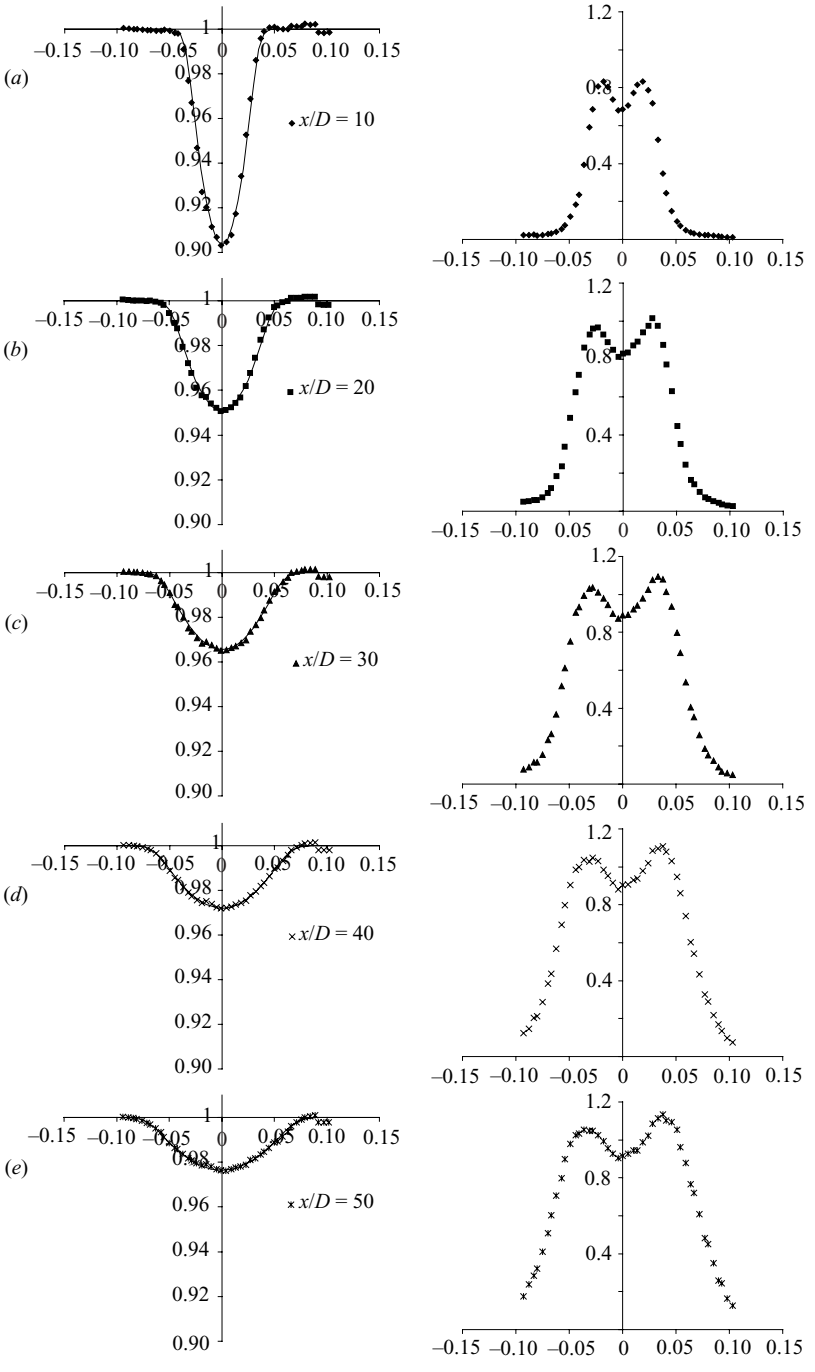

FIGURE 6. Mean velocity profiles and root mean square of the velocity vs. r. (a) $x/D = 10$, (b) 20, (c) 30, (d) 40, (e) 50.

obtained from the fixed rake. Here, all the probes were connected to the same brand of anemometer (DANTEC). The probe labelled 1 in figure 4 shows least agreement to the curve fit. This probe was connected to one of the AN1003 channels, which is

the main reason for it behaving differently because of the different characteristics of the anemometer. Note that the velocity differences are extremely small. The difference in velocity measured by probes 1 and 2 is 0.4 % of the free-stream velocity. The same trend is seen for probes 1, 3, 5 and 6, which are also connected to AN1003 anemometers. But clearly, it is probe 1 that deviates the most. The solid lines in the figure show the curve fit explained in Appendix B. All profiles show very good agreement to this fit. The centring of the rake is seen to have been performed in a satisfactory manner. Note that the right-hand side of the measured positions, positive r, extends to larger radius than the curve for negative r, since the entire probe rake was traversed to two positions in the positive r-direction (5 and 10 mm) to fill out the profiles as mentioned in § 4.5.

The further evolution of the mean velocity profiles for $x/D = 60$ to 150 is shown in figures 7 and 8. For these positions, the mean velocity deficit continues to fall, from 2 % at $x/D = 60$ to about 1.1 % at $x/D = 150$. The curve fits continue to be in very good agreement with the measured points, especially for negative r. As noted above, probe 1 continues to be off the curve. The probe rake centring is still found to be accurate, ensuring that the flow direction in the wind tunnel test section is uniform within the accuracy of the experiment, so no re-centring of the probe rakes was found necessary. For the later positions, it is clear from the curve fits that the outermost point is not located in the free stream. Hence, the curve fit is essential in the estimation of the mean velocity deficit.

The normalized mean velocity deficit profiles, $(U_\infty - U(r))/U_o$, are plotted versus r/δ_* in figure 9. In this figure, all profiles obtained with the probes on the fixed rake (negative r) show a remarkable collapse. The previously identified problematic probe 1 in the outer part of the movable rake shows least agreement to the profile. In fact, the points measured by this probe seem to fall on a curve of their own, slightly elevated from the curve that ties all the others together. It would be very tempting to just shift these points to fall on top of the curve fit (or omit these data entirely). Also, the increased scatter for positive r is due to probes 1, 3, 5, and 6 that are connected to AN1003 anemometers, which have a different thermal drift characteristic from those of 54T40.

Figure 9 also gives an indication of why previous experiments show large scatter in the mean velocity profiles (if they show profiles at all), since the largest deviation in figure 9 is only 0.4 % of the mean velocity. If a probe rake had not been used, the accuracy would have been even more seriously affected by the anemometer drift, since the profile would have been obtained by traversing a single probe through the wake. If the traversing were made at random positions spanning the wake, the thermal drift of the anemometers would have shown up as increased scatter in the profiles. Or if the traversing were sequential, the profiles would have been significantly skewed. The measurements of very small mean velocity differences in the wake are indeed very difficult to make correctly, but made possible in this experiment by simultaneously measuring with a large number of probes and many nearly identical anemometers.

6. Streamwise variation of scaling parameters

The scaling parameters obtained through the regressive fit described in Appendix B, the centreline mean velocity deficit, U_o, and the lateral wake width, δ_*, clearly provide the collapse of the mean velocity profiles as shown in figure 9. The streamwise variation of the mean velocity deficit is shown in figure 10. It is clear that U_o

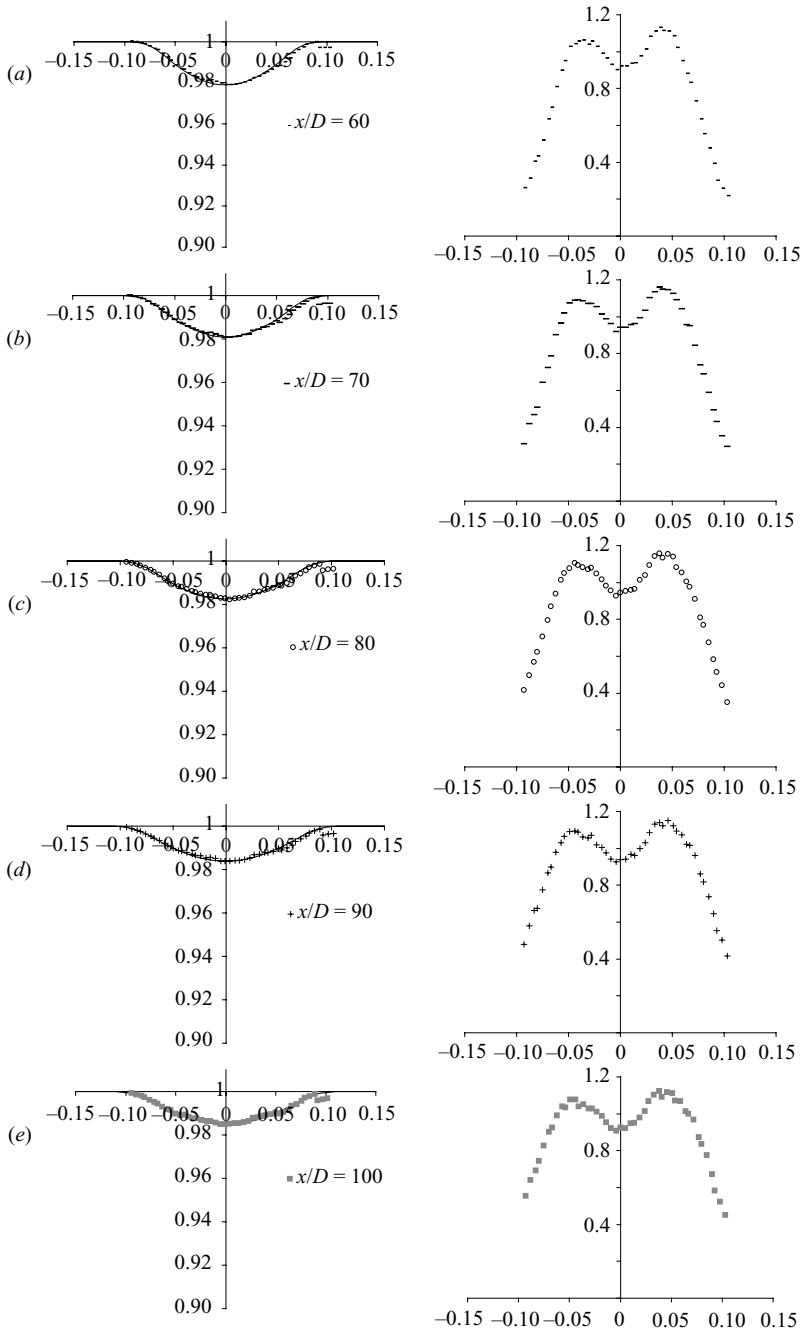

FIGURE 7. Mean velocity profiles and root mean square of the velocity vs. r. (a) $x/D = 60$, (b) 70, (c) 80, (d) 90, (e) 100.

decreases monotonically and in a smooth manner. The solid line shows the high-Reynolds-number equilibrium similarity solution discussed below in equation (8.2).

In figure 11, the streamwise evolution of the lateral length scale, δ_*, defined by equation (2.4) is shown. It is seen from this figure that δ_* grows monotonically

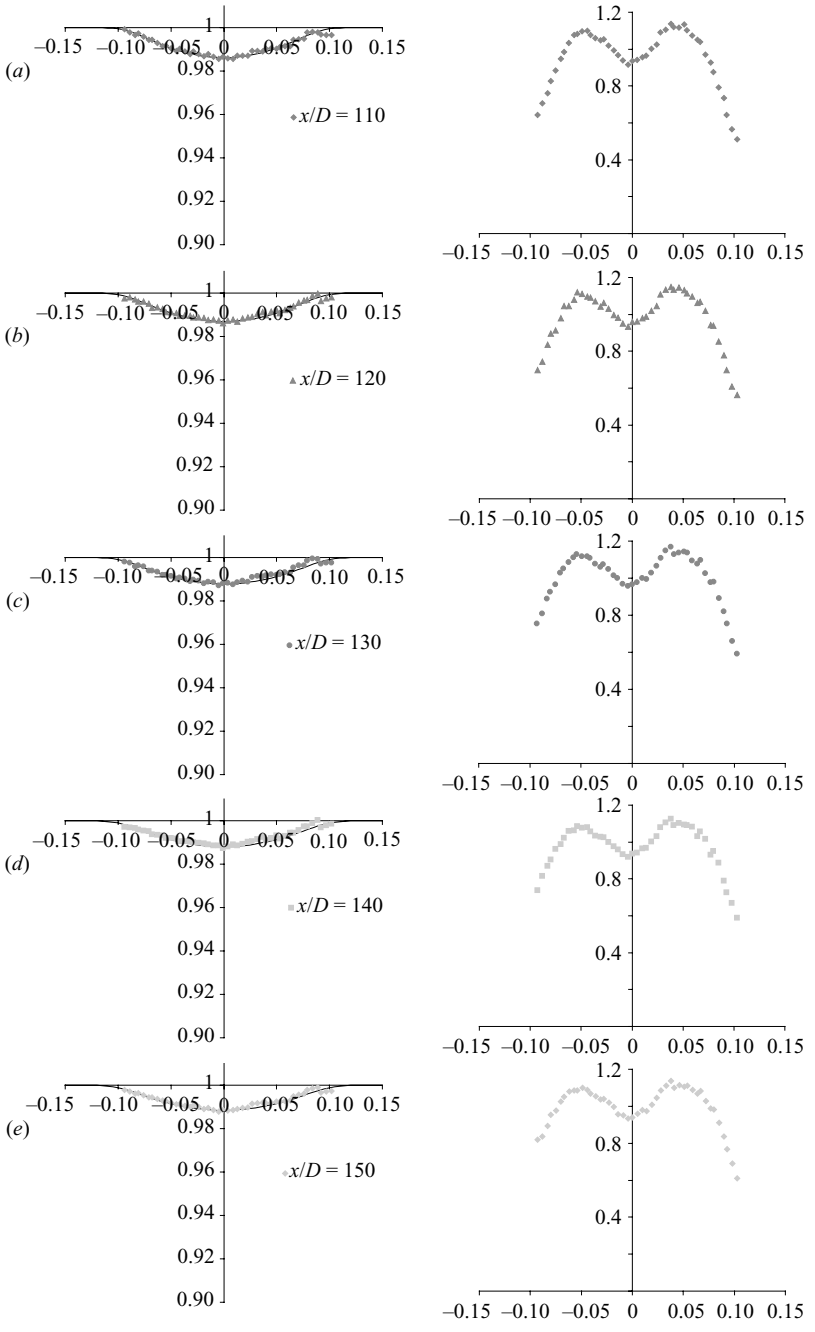

FIGURE 8. Mean velocity profiles and root mean square of the velocity vs. r. (a) $x/D = 110$, (b) 120, (c) 130, (d) 140, (e) 150.

from about 3θ (17 mm), or slightly less than the disk diameter at $x/D = 10$, to about 9θ (50 mm) or 2.5 times the disk diameter at $x/D = 150$. The solid line shows the high-Reynolds-number equilibrium similarity solution discussed below in equation (8.1).

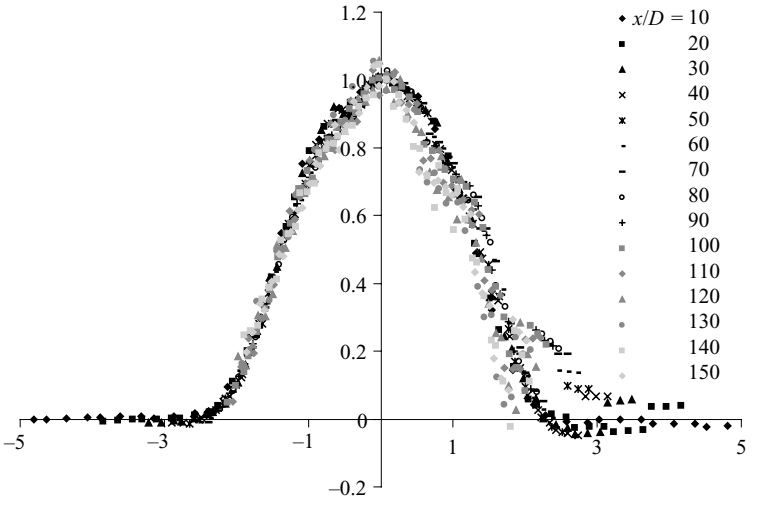

FIGURE 9. Normalized mean velocity profiles, $(U_\infty - U(r))/U_o$ vs. r/δ_*.

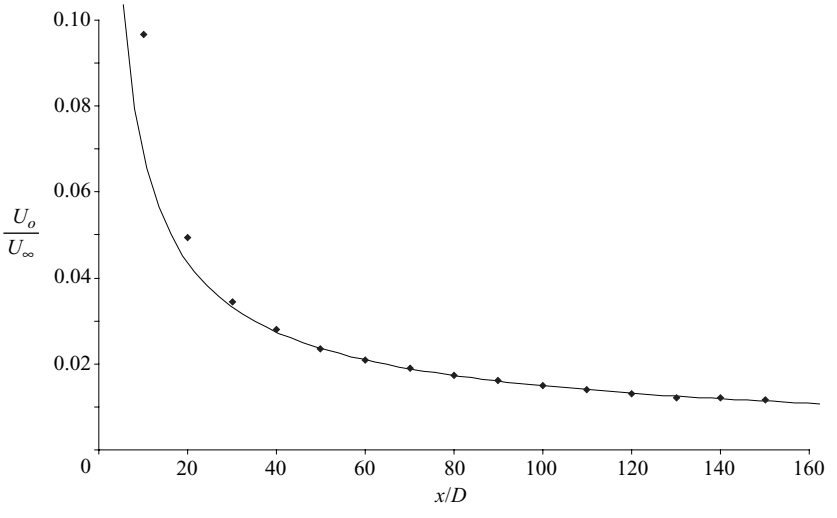

FIGURE 10. Downstream evolution of the centreline velocity deficit, U_o/U_∞ vs. x/D.

These two scaling parameters, U_o and δ_*, can be used to obtain the *local* Reynolds number of the flow, $R = U_o\delta_*/\nu$. The downstream variation of the local Reynolds number is shown in figure 12. Clearly it decreases with downstream distance, which distinguishes this flow from most other free shear flows where the local Reynolds number either increases or remains constant. In fact, it is this decreasing local Reynolds number which is the reason for the existence of two different equilibrium similarity solutions for the axisymmetric wake, one for high and one for low Reynolds number, see George (1989) and Johansson *et al.* (2003). The hatched line in the figure marks the approximate value of the local Reynolds number where the high-Reynolds-number equilibrium similarity solution ceases to be valid, and viscous effects drive the flow to its other turbulent state as discussed in detail by Johansson *et al.* (2003).

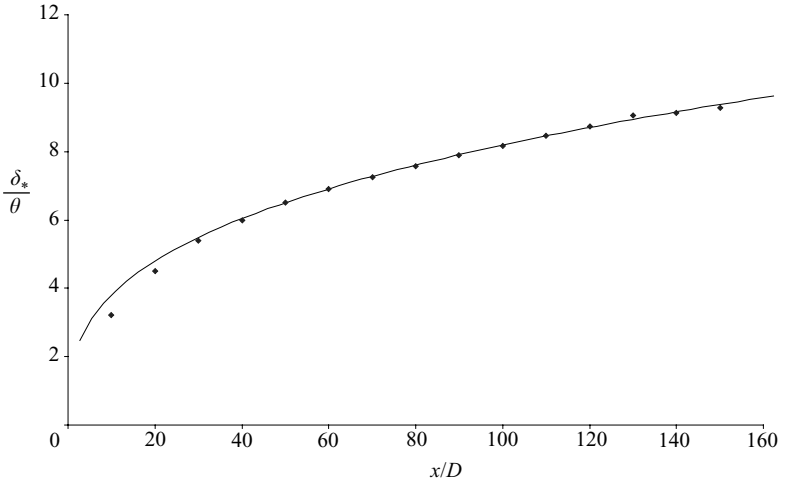

FIGURE 11. Downstream evolution of the lateral wake length scale, δ_*/θ, vs. x/D.

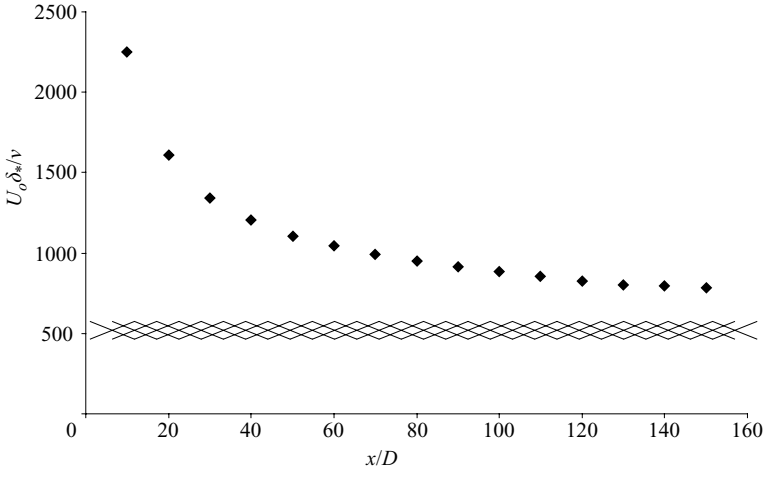

FIGURE 12. Downstream evolution of the local Reynolds number, $U_o\delta_*/\nu$, vs. x/D.

In this experiment, the local Reynolds number falls from 2234 at $x/D = 10$, to 774 at $x/D = 150$, which is well above the suggested threshold of 500 below which the high-Reynolds-number solution does not apply.

7. Turbulence intensity profiles

The reason for the r.m.s. velocity not being so sensitive to the thermal drift of the anemometers can also be seen in figure 5. Although the calibration curves are shifted from one time to another, the slopes are nearly unchanged. For such weak fluctuations, the fluctuating velocity is proportional to the fluctuating voltage times the derivative of the function that relates voltage and velocity (see Perry (1982) for a more detailed discussion). Thus the fluctuating part of the velocity is hardly affected, while the mean is seriously compromised. But there remains a problem for the turbulence

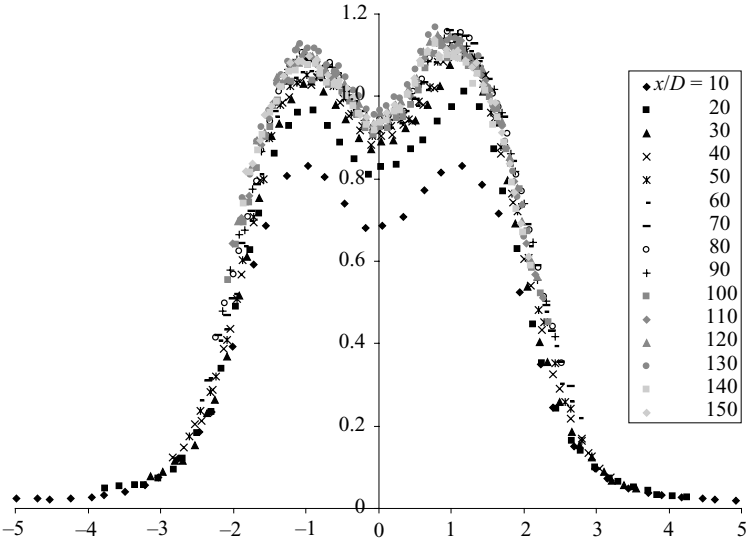

FIGURE 13. Normalized turbulence intensity profiles, u'/U_o vs. r/δ_*.

intensities, since the r.m.s. values must be divided by the centreline mean velocity deficit, which is the least accurately determined quantity. It is the constancy (or lack thereof) of u'/U_o that is the surest indicator of a similarity scaling regime, so even the establishment of flow regime is affected by to the drift problem.

The root mean square of the fluctuations, u', is shown for the downstream positions of $x/D = 10$, 20, 30, 40, and 50 in figure 6. Here, u' is normalized by the centreline mean velocity deficit determined above. As with the mean velocity profiles, the radial direction is left unscaled to show the profile width in physical dimensions. As is clear in figure 6, the hot-wire array almost covers the whole wake, since the tails of the u'/U_∞ profiles go to a value just below 0.1 %. The tunnel free-stream turbulence intensity with an empty test section is reported by Johansson (2002) to be less than 0.03 %. Figure 6 further supports the indications provided by the study of the mean velocity profiles in the previous section that the rakes were properly centred. The apparent slightly higher peak value on the right-hand side is due to one probe. The probes that prevent the profiles from being smooth are the ones numbered 0, 1, 3, 5, and 6, all connected to AN1003 anemometers. But the effects of the different anemometers are not as pronounced as for the mean velocity profiles.

Figures 7 and 8 show the downstream evolution of the turbulence intensities between $60 \leqslant x/D \leqslant 150$. Here, the peak values (as well as the centreline values) of u'/U_o have reached a constant level, and remain constant for all the remaining measured downstream positions. The profiles eventually start to show more scatter, but it must be noted that the ratio of u'/U_∞ has dropped to below 1.3 % at $x/D = 150$.

The normalized turbulence intensity profiles for all downstream locations are shown in figure 13, i.e. u'/U_o vs. r/δ_*. These profiles collapse quite well for all downstream positions greater than about $x/D = 30$. This is remarkable, considering the difficulties in obtaining correct mean velocity profiles using the different anemometer systems described above. Clearly, as expected, the thermal drift of the anemometers has very little direct influence on fluctuating quantities. This is especially important for Part 2 of this investigation which uses the cross-spectra in conjunction with the proper orthogonal decomposition.

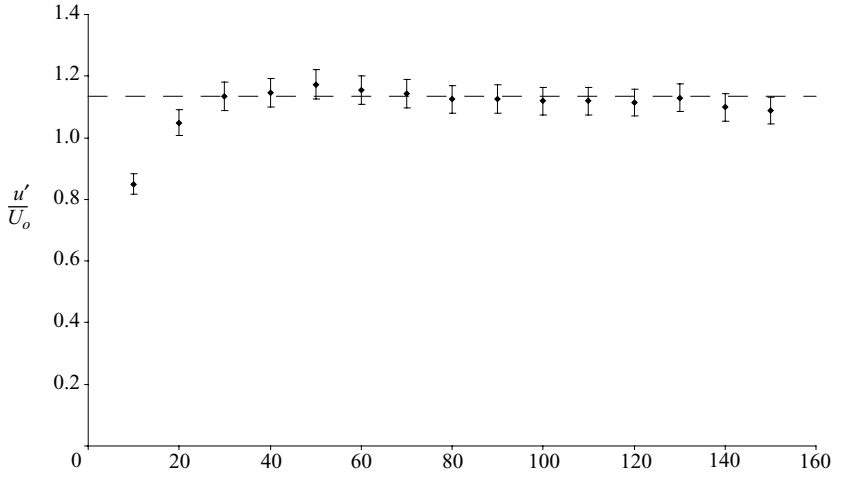

FIGURE 14. Downstream evolution of the normalized turbulence intensity, u'/U_o, vs. x/D.

The downstream evolution of the maximum of the normalized turbulence intensities is shown in figure 14. Here, it is further highlighted that the ratio u'/U_o approaches a constant value which is reached approximately at $x/D = 30$ for this wake generator. This ratio remains constant throughout the downstream positions covered in this experiment. This is of considerable importance in establishing the existence of the high-Reynolds-number equilibrium similarity regime as noted below. The points presented are the average of the peak values from either side of the centreline shown in figure 13. The error bars indicate an uncertainty of $\pm 2\,\%$, which covers both peak values.

8. High-Reynolds-number similarity solution

The high-Reynolds-number similarity theory of George (1989) and Johansson *et al.* (2003) predicts that the evolution of the scaling parameters U_o and δ_* should behave as

$$\frac{\delta_*}{\theta} = a\left[\frac{x - x_o}{\theta}\right]^{1/3} \tag{8.1}$$

$$\frac{U_o}{U_\infty} = b\left[\frac{x - x_o}{\theta}\right]^{-2/3} \tag{8.2}$$

where the virtual origin must be the same for both; and the parameters a, b, and x_o can depend on the wake generator, but must satisfy the momentum constraint $a^2 b = 1$. Johansson *et al.* (2003) suggest that this theory should apply only after the initial transient has decayed and only as long as the local Reynolds number is greater than 500 (i.e. $R = U_o\delta_*/\nu > 500$). They further suggest that the best measure of when the initial transients have died out is when $u'/U_o =$ constant, as required by application of the equilibrium similarity theory to the kinetic energy equation. From figure 14, it is clear that this condition is satisfied for $x/D > 30$ for this experiment. Moreover, from figure 12, $R > 500$ for all downstream positions. Therefore, if any data were in agreement with the high-Reynolds-number solution, it should be these.

They are. The solid lines on figures 10 and 11 show fits of equations (8.2) and (8.1) to the experimental data. The agreement is excellent. Linear regression yields values

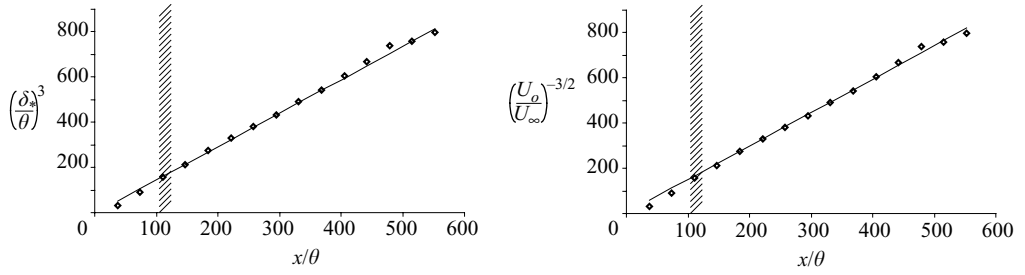

FIGURE 15. $(\delta_*/\theta)^3$ and $(U_o/U_\infty)^{-3/2}$ vs. x/θ.

for the constants as: $a = 1.14$, $b = 0.77$, and $x_o = -2.4\theta$. An even stronger indication of the agreement between theory and data is provided by the plots of $(\delta_*/\theta)^3$ and $(U_o/U_\infty)^{-3/2}$ versus x/θ in figure 15. These plots do not depend on a virtual origin, but clearly are linear for $x/\theta > 120$ ($x/D > 30$).

The collapse of the mean velocity and intensity profiles in figures 9 and 13 is further confirmation of both the equilibrium similarity theory and the experiment. Note, the curve fits used for the regressive fits to the velocity profiles did not assume similarity, but optimized the choice of parameters for each position downstream. The equilibrium similarity theory also predicts that the individual curves described in Appendix B should collapse, and to an excellent approximation they do.

9. Power spectral densities

Power spectral densities were obtained for downstream positions of $x/D = 50$, 70, 90, 110, 130, and 150. As mentioned in § 4.3, these data were obtained from a much more extensive data set than for the mean and r.m.s. values considered above. The downstream evolution of the power spectra for each radial position in the wake covered by the fixed hot-wire rake is shown in figure 16. The power spectra for each radius shown in figure 16 are the averaged values of the probes located on the same radius as the fixed and movable rake. It is clear from these plots that the peak at the Strouhal number 0.13 is visible in all off-centre spectra for all downstream positions. Thus, this feature remains in the flow for a substantial distance downstream. It is noticeable also that the frequency is not changing at all with downstream distance, confirming the findings of Cannon, Champagne & Glezer (1993) that this is truly a convected structure. No peak at this frequency appears in the spectra at the centreline (a certain confirmation of a properly centred disk, since it will be shown in Part 2 to be both transient and associated with azimuthal mode-1).

Using the obtained scaling parameter δ_* and applying Taylor's frozen field hypothesis with the convection velocity taken as the free-stream velocity, the spectra at the centreline were normalized. These are shown in figure 17. Here, it is very clear that this normalization collapses the spectra for high wavenumbers. Taylor's hypothesis is not in general valid for low wavenumbers, as pointed out by Lumley (1967), but it is remarkable how different the spectra are for low wavenumbers. It is not at all clear from this single-point statistical investigation what causes this behaviour. This is investigated further in Part 2 using multi-point statistics and POD.

Finally, a very clear inertial subrange is visible, especially in figure 17. This is exactly as predicted by Johansson *et al.* (2003), who argued that the existence of such an inertial subrange in the spectrum was a necessary condition for the applicability of the high-Reynolds-number solution. Because of the wire roll-off and sampling rate,

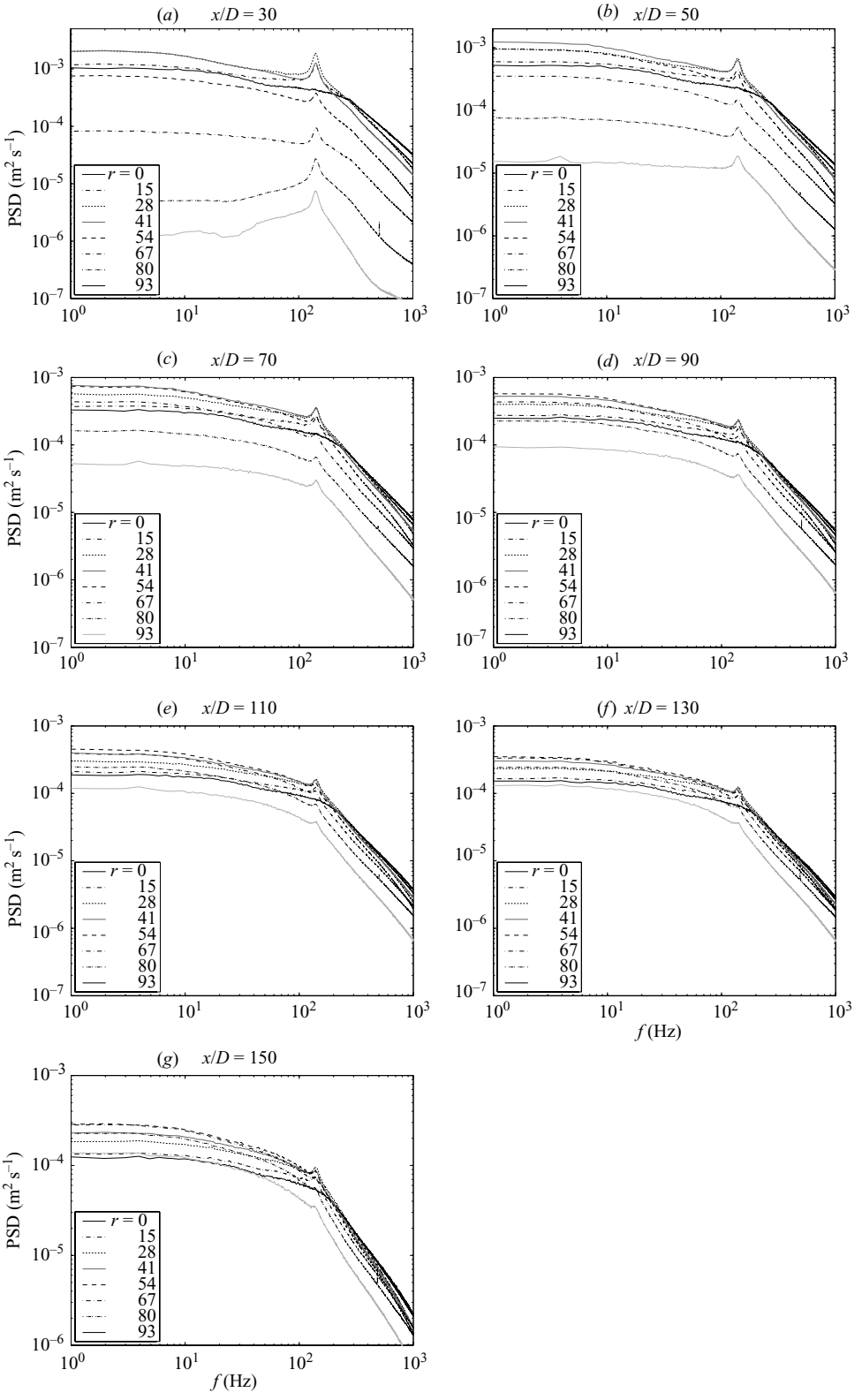

FIGURE 16. Power spectral densities at each radius of the wake at different positions: (*a*) $x/D = 30$, (*b*) 50, (*c*) 70, (*d*) 90, (*e*) 110, (*f*) 130, and (*g*) 150.

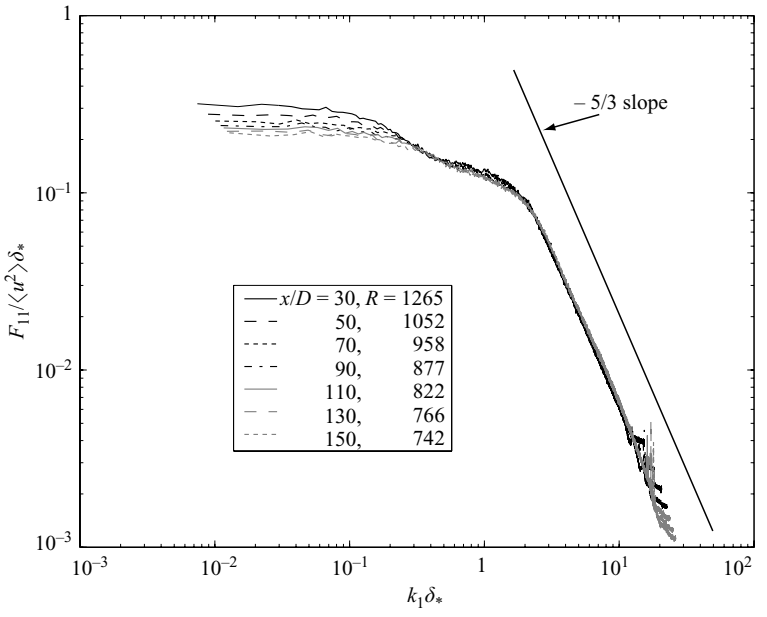

FIGURE 17. Normalized wavenumber spectra at the centreline.

it is not clear how far this inertial subrange extends. This experiment was originally designed to capture the large-scale, energy-containing scales, which is the reason for the spectra being cut at relatively low wavenumbers. If the high-wavenumber dissipative range were to be investigated, much smaller hot wires would have to be used to increase the resolution.

10. Summary

In this paper, the high-Reynolds-number wake behind a disk has been investigated using rakes of hot-wire probes. The initial Reynolds number was 26 400. The measurement downstream range was $10 \leqslant x/D \leqslant 150$ ($36 \leqslant x/\theta \leqslant 552$). It was found that in spite of the limitations imposed by anemometer drift, the accuracy of mean velocity profiles can be substantially improved by using regression techniques to fit the simultaneous data from rakes of hot wires to an assumed profile shape.

A number of open questions from earlier investigations has been resolved. It has been shown that the turbulence intensity ratio u'/U_o really does reach a constant value. This happens once the initial transients have settled, which can take a substantial distance downstream ($x/D > 30$ in this investigation). Moreover, it has been shown that this flow satisfied all necessary conditions for the high-Reynolds-number equilibrium similarity analysis of Johansson *et al.* (2003) to apply, most notably that the local Reynolds number be greater than 500 throughout the entire experiment, that the spectra exhibit an inertial subrange, and that u'/U_o has reached a constant value. Corresponding to this, the wake half-width grows as $(x - x_o)^{1/3}$ and the velocity deficit decreases as $(x - x_o)^{-2/3}$, albeit with coefficients and virtual origin uniquely determined by the generator. The data and theory are in excellent agreement.

The authors would like to thank Professor Henrik Alfredsson of the Swedish Royal Institute of Technology (KTH) for the use of the MTL wind tunnel. The first author would also especially like to thank Mr Davide Medici for sharing the tunnel time and for the company during the experiment. This work was initially supported by Chalmers University of Technology. It continues with the support of the Swedish Research Council, grant number 2641.

Appendix A. The effect of a free-stream pressure gradient

When a pressure gradient in the free-stream direction is taken into account, the momentum equation (to second order in the turbulence intensity) is

$$U\frac{\partial U}{\partial x}+V\frac{\partial U}{\partial r}=-\frac{1}{r}\frac{\partial}{\partial r}(r\overline{uv})-\frac{1}{\rho}\frac{\partial P_\infty}{\partial x}. \tag{A 1}$$

Assuming the free stream to be inviscid and non-turbulent, the balance there is given by Euler's equation as

$$-\frac{1}{\rho}\frac{\partial P_\infty}{\partial x}=U_\infty\frac{\partial U_\infty}{\partial x}, \tag{A 2}$$

where both P_∞ and U_∞ depend (to leading order) only on the streamwise coordinate.

Using continuity (multiplied by $(U-U_\infty)$) and equation (A 2), equation (A 1) can be rewritten as

$$\frac{\partial}{\partial x}\left[U\left(U-U_\infty\right)\right]+\left(U-U_\infty\right)\frac{\partial U_\infty}{\partial x}+\frac{1}{r}\frac{\partial}{\partial r}\left[rV\left(U-U_\infty\right)\right]=-\frac{1}{r}\frac{\partial}{\partial r}\left(r\overline{uv}\right). \tag{A 3}$$

This can be integrated across the flow to obtain:

$$\frac{\mathrm{d}}{\mathrm{d}x}\left[\int_0^\infty U\left(U-U_\infty\right)r\,\mathrm{d}r\right]+\frac{\mathrm{d}U_\infty}{\mathrm{d}x}\int_0^\infty\left(U-U_\infty\right)r\,\mathrm{d}r=0. \tag{A 4}$$

Clearly the second integral accounts for the external pressure gradient and vanishes identically if it is zero; so that the equation reduces to equation (2.2) in the limit of $|U-U_\infty|\ll U_\infty$. Using the definitions of θ and δ_* (equations (2.3) and (2.4)), equation (A 4) can be rewritten as

$$\frac{\mathrm{d}}{\mathrm{d}x}(U_\infty^2\theta)+\delta_* U_o\frac{\mathrm{d}U_\infty}{\mathrm{d}x}=0 \tag{A 5}$$

which in turn can be integrated to yield

$$U_\infty^2\theta+\int_0^x\left[\delta_* U_o\frac{\mathrm{d}U_\infty}{\mathrm{d}x}\right]\mathrm{d}x'=\text{constant}=\text{drag}. \tag{A 6}$$

For this particular experiment, the two terms of equation (A 6) are shown in figure 18. The second term is less than 0.1 % of the first, and hence clearly negligible.

Appendix B. Correction for anemometer drift

The correction method for taking the thermal drift of the anemometers into account was applied in the following steps:

(*a*) A wake profile of the form $\exp(-r^2)$ (which corresponds to the constant-eddy-viscosity solution, cf. the appendix of Johansson *et al.* 2003) undershoots the data points near the centreline, and falls off too slowly for large r. A more general curve

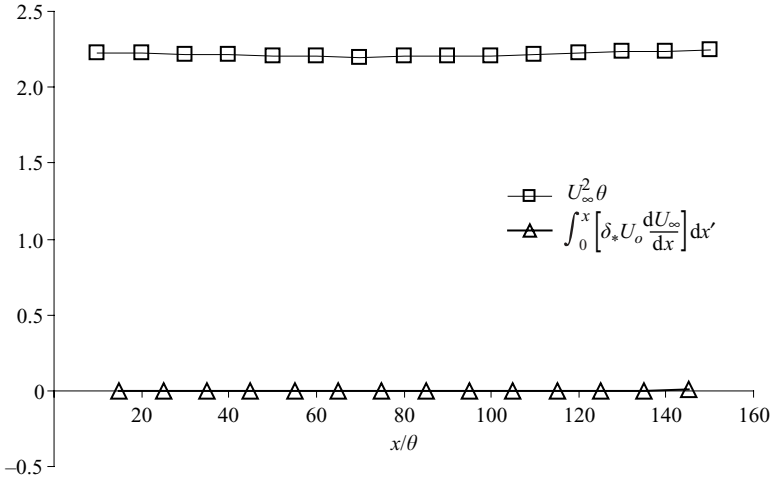

FIGURE 18. Terms in equation (A 6).

which provides an excellent fit to all profiles is given by

$$U_{fs} - U(r) = (U_{fs} - U_{CL})(1 + C_2 r^2 + \cdots + C_n r^n)\exp(-D_2 r^2 - D_4 r^4), \qquad (B\,1)$$

where n is an integer multiple of 2. The sufficient order of the polynomial was found to be $n = 4$. U_{fs} denotes the apparent free-stream velocity that will deviate from the correct free-stream velocity, U_∞, because of the thermal drift of the anemometers. Thus, the free parameters of the curve fit are U_{fs}, C_2, C_4, D_2, and D_4, while U_{CL} and $U(r)$ are the values obtained from the experiment. Note that U_{fs} simply shifts the whole velocity profile up and down.

(*b*) The curve fit for each position (that covered the wake enough to permit an estimate of the momentum from a direct integration of data) was integrated to check whether the flow conserved momentum. This was found to be the case from the first measured downstream position, $x/D = 10$ to $x/D = 50$.

(*c*) Since the flow was found to conserve momentum, the link between the velocity deficit scale and the lateral length scale was known. This relation, $U_o\delta_*^2 = U_\infty\theta^2$, had to be satisfied at all downstream locations. Hence, the curve fit was modified to be valid for all downstream positions simultaneously, by rewriting equation (B 1) as

$$U_{fs} - U(r) = (U_{fs} - U_{CL})(1 + A(r/\delta_*)^2 + B(r/\delta_*)^4)\exp(-C(r/\delta_*)^2 - D(r/\delta_*)^4). \quad (B\,2)$$

Here, A, B, C, D are now constants common for all the velocity profiles. A regressive scheme was also used to fit equation (B 2) to the measured profiles, with the added constraint of momentum conservation. This resulted in values of δ_* for all the downstream locations, from which the velocity scale, U_o, could be computed. The values for the general profile constants were found to be: $A =$,0.049, $B = 0.128$, $C = 0.345$, and $D = 0.134$.

REFERENCES

CANNON, S. C. 1991 Large-scale structures and the spatial evolution of wakes behind axisymmetric bluff bodies. PhD thesis, Dept. of Aerospace and Mechanical Engineering University of Arizona.

CANNON, S., CHAMPAGNE, F. & GLEZER, A. 1993 Observations of large-scale structures in wakes behind axisymmetric bodies. *Exps. Fluids* **14**, 447–450.

Carmody, T. 1964 Establishment of the wake behind a disk. *Trans. ASME. J. Basic Engng* **86**, 869–882.

Cooper, R. D. & Lutzky, M. 1955 Exploratory investigation of the turbulent wakes behind bluff bodies. *DTMB Rep.* 963.

Gamard, S., Jung, D., Woodward, S. & George, W. K. 2002 Application of a 'slice' POD to the far field of an axisymmetric turbulent jet. *Phys. Fluids* **14** (7), 2515–2522.

George, W., Beuther, P. D. & Shabbir, A. 1989 Polynomial calibrations for hot-wires in thermally varying flows. *J. Expl. Therm. Fluid Sci.* **2**, 230–235.

George, W. K. 1989 The self-preservation of turbulent flows and its relation to initial conditions and coherent structures. In *Advances in Turbulence* (ed. W. K. George & R. E. A. Arndt), pp. 39–73. Hemisphere.

Gibson, C. H., Chen, C. C. & Lin, S. C. 1968 Measurements of turbulent velocity and temperature fluctuations in the wake of a sphere. *AIAA J.* **6**, 642–649.

Glauser, M. & George, W. 1987 Orthogonal decomposition of the axisymmetric jet mixing layer including azimuthal dependence. In *Advances in Turbulence* (ed. G. Comte-Bellot & J. Mathieu), pp. 357–366. Spring.

Gourlay, M. J., Arendt, S. C., Fritts, D. C. & Werne, J. 2001 Numerical modeling of initially turbulent wakes with net momentum. *Phys. Fluids* **13**, 3783–3802.

Hwang, N. C. H. & Baldwin, L. V. 1966 Decay of turbulence in axisymmetric wakes. *Trans. ASME: J. Basic Engng* **88**, 261–268.

Johansson, A. V. 1992 A low speed wind-tunnel with extreme flow quality - design and tests. In *Prog. ICAS Congress 1992*, pp. 1603–1611. ICAS-92-3.8.1.

Johansson, P. B. V. 2002 The axisymmetric turbulent wake. PhD thesis, Chalmers University of Technology, Gothenburg, Sweden.

Johansson, P. B. V. & George, W. K. 2006 The far downstream evolution of the high-Reynolds-number axisymmetric wake hehind a disk. Part 2. Slice proper orthogonal decomposition. *J. Fluid Mech.* **555**, 387–408.

Johansson, P. B. V., George, W. K. & Gourlay, M. J. 2003 Equilibrium similarity, effects of initial conditions and local Reynolds number on the axisymmetric wake. *Phys. Fluids.* **15**, 603–617.

Johansson, P. B. V., George, W. K. & Woodward, S. H. 2002 Proper orthogonal decomposition of an axisymmetric turbulent wake behind a disk. *Phys. Fluids* **14** (7), 2508–2514.

Lumley, J. L. 1967 The inertial subrange in nonequilibrium turbulence. In *Atmospheric Turbulence and Radio Wave Propagation* (ed. A. M. Yaglom & V. I. Tatarsky), pp. 157–164. Moscow, USSR: Nauka.

Perry, A. 1982 *Hot Wire anemometry*. Clarendon.

Uberoi, M. S. & Freymuth, P. 1970 Turbulent energy balance and spectra of the axisymmetric wake. *Phys. Fluids* **13** (9), 2205–2210.